Digital holographic reflectometry

Tristan Colomb[1], Stefan Krivec[2,3], Herbert Hutter[2], Ahmet Ata Akatay[4], Nicolas Pavillon[4], Frédéric Montfort[1], Etienne Cuche[1], Jonas Kühn[5], Christian Depeursinge[4], Yves Emery[1]

[1]*Lyncée Tec SA, PSE-A, CH-1015 Lausanne, Switzerland*
tristan.colomb@lynceetec.com

http://www.lynceetec.com

[2]*KAI Kompetenzzentrum Automobil- und Industrieelektronik, Europastrasse 8, A-9524 Villach, Austria*

[3]*Technische Universität Wien; Institut für Chemische Technologien und Analytik, Getreidemarkt 9/164-AC, A-1060 Wien, Austria*

[4] *Advanced Photonics Laboratory, Ecole Polytechnique Fédérale de Lausanne, CH-1015 Lausanne, Switzerland*

[5] *DP-CHUV, Site de Cery, 1008 Prilly, Switzerland*

Abstract: Digital holographic microscopy (DHM) is an interferometric technique that allows real-time imaging of the entire complex optical wavefront (amplitude and phase) reflected by or transmitted through a sample. To our knowledge, only the quantitative phase is exploited to measure topography, assuming homogeneous material sample and a single reflection on the surface of the sample. In this paper, dual-wavelength DHM measurements are interpreted using a model of reflected wave propagation through a three-interfaces specimen (2 layers deposited on a semi-infinite layer), to measure simultaneously topography, layer thicknesses and refractive indices of micro-structures. We demonstrate this DHM reflectometry technique by comparing DHM and profilometer measurement of home-made SiO_2/Si targets and Secondary Ion Mass Spectrometry (SIMS) sputter craters on specimen including different multiple layers.

OCIS codes: (090.1995) Digital holography; (120.1840) Densitometers, reflectometers; (120.5700) Reflection; (230.4170) Multilayers; (310.0310) Thin films

References and links

1. E. Cuche, P. Marquet, and C. Depeursinge, "Simultaneous amplitude-contrast and quantitative phase-contrast microscopy by numerical reconstruction of Fresnel off-axis holograms," Appl. Opt. **38**, 6994–7001 (1999). URL http://www.opticsinfobase.org/ao/abstract.cfm?URI=ao-38-34-6994.
2. S. de Nicola, P. Ferraro, A. Finizio, S. Grilli, G. Coppola, M. Iodice, P. De Natale, and M. Chiarini, "Surface topography of microstructures in lithium niobate by digital holographic microscopy," Meas. Sci. Technol. **15**, 961–968 (2004).
3. J. Kühn, F. Charrière, T. Colomb, E. Cuche, F. Montfort, Y. Emery, P. Marquet, and C. Depeursinge, "Axial sub-nanometer accuracy in digital holographic microscopy," Meas. Sci. Technol. **19**, 074,007–74,008 (2008).
4. T. Ikeda, G. Popescu, R. Dasari, and M. Feld, "Hilbert phase microscopy for investigating fast dynamics in transparent systems," Opt. Lett. **30**, 1165–1167 (2005).

#121163 - $15.00 USD Received 8 Dec 2009; revised 2 Feb 2010; accepted 3 Feb 2010; published 5 Feb 2010

5. P. Marquet, B. Rappaz, P. Magistretti, E. Cuche, Y. Emery, T. Colomb, and C. Depeursinge, "Digital holographic microscopy: a noninvasive contrast imaging technique allowing quantitative visualization of living cells with subwavelength axial accuracy," Opt. Lett. **30**, 468–470 (2005). URL http://www.opticsinfobase.org/ol/abstract.cfm?URI=ol-30-5-468.
6. B. Rappaz, A. Barbul, Y. Emery, R. Korenstein, C. Depeursinge, P. Magistretti, and P. Marquet, "Comparative study of human erythrocytes by digital holographic microscopy, confocal microscopy, and impedance volume analyzer," Cytometry Part A **73a**, 895–903 (2008).
7. B. Rappaz, F. Charrière, C. Depeursinge, P. Magistretti, and P. Marquet, "Simultaneous cell morphometry and refractive index measurement with dual-wavelength digital holographic microscopy and dye-enhanced dispersion of perfusion medium," Opt. Lett. **33**, 744–746 (2008). URL http://www.opticsinfobase.org/ol/abstract.cfm?URI=ol-33-7-744.
8. H. Wahba and T. Kreis, "Characterization of graded index optical fibers by digital holographic interferometry," Appl. Opt. **48**, 1573–1582 (2009). URL http://www.opticsinfobase.org/ao/abstract.cfm?URI=ao-48-8-1573.
9. C. Yelleswarapu, S.-R. Kothapalli, and D. Rao, "Optical Fourier techniques for medical image processing and phase contrast imaging," Opt. Commun. **281**, 1876–1888 (2008).
10. C. Moore, "Optical reflectometry elucidates layer thicknesses," III-Vs Review **12**, 34–37 (1999).
11. P. Hlubina, J. Lunacek, D. Ciprian, and R. Chlebus, "Spectral interferometry and reflectometry used to measure thin films," Applied Physics B: Lasers and Optics **92**, 203–207 (2008).
12. S. Debnath, M. Kothiyal, J. Schmit, and P. Hariharan, "Spectrally resolved white-light phase-shifting interference microscopy for thickness-profile measurements of transparent thin film layers on patterned substrates," Opt. Express **14**, 4662 (2006). URL http://www.opticsinfobase.org/oe/abstract.cfm?URI=oe-14-11-4662.
13. S. K. Debnath, J. Kothiyal, Mahendra P.and Schmit, and P. Hariharan, "Spectrally resolved phase-shifting interferometry of transparent thin films: sensitivity of thickness measurements," Appl. Opt. **45**, 8636–8640 (2006). URL http://www.opticsinfobase.org/ao/abstract.cfm?URI=ao-45-34-8636.
14. J. Kühn, T. Colomb, F. Montfort, F. Charrière, Y. Emery, E. Cuche, P. Marquet, and C. Depeursinge, "Real-time dual-wavelength digital holographic microscopy with a single hologram acquisition," Opt. Express **15**, 7231–7242 (2007). URL http://www.opticsinfobase.org/oe/abstract.cfm?URI=oe-15-12-7231.
15. C. Mann, L. Yu, C.-M. Lo, and M. Kim, "High-resolution quantitative phase-contrast microscopy by digital holography," Opt. Express **13**, 8693–8698 (2005). URL http://www.opticsinfobase.org/oe/abstract.cfm?URI=oe-13-22-8693.
16. E. Cuche, P. Marquet, and C. Depeursinge, "Spatial filtering for zero-order and twin-image elimination in digital off-axis holography." Appl. Opt. **39**, 4070–4075 (2000). URL http://www.opticsinfobase.org/ao/abstract.cfm?URI=ao-39-23-4070.
17. T. Colomb, J. Kühn, F. Charrière, C. Depeursinge, P. Marquet, and N. Aspert, "Total aberrations compensation in digital holographic microscopy with a reference conjugated hologram," Opt. Express **14**, 4300–4306 (2006). URL http://www.opticsinfobase.org/oe/abstract.cfm?URI=oe-14-10-4300.
18. T. Colomb, F. Montfort, J. Kühn, N. Aspert, E. Cuche, A. Marian, F. Charrière, S. Bourquin, P. Marquet, and C. Depeursinge, "Numerical parametric lens for shifting, magnification and complete aberration compensation in digital holographic microscopy," JOSA A **23**, 3177–3190 (2006). URL http://www.opticsinfobase.org/josaa/abstract.cfm?URI=josaa-23-12-3177.
19. P. Pereyra and A. Robledo-Martinez, "On the equivalence of the summation and transfer-matrix methods in wave propagation through multilayers of lossless and lossy media," Eur. J. Phys. **30**, 393–401 (2009).
20. C. Cobianu, C. Pavelescu, and A. Paunescu, "The effect of deposition conditions on the refractive index of LTCVD SiO2 films," Journal of Materials Science Letters **4**, 1419–1420 (1985).
21. URL http://refractiveindex.info/.
22. D. S. McPhail, "Applications of Secondary Ion Mass Spectrometry (SIMS) in Materials Science," Journal of Materials Science **41**, 873–903 (2006).
23. Y. Yamamura and M. Ishida, "Simulation of oxide sputtering and SIMS depth profiling of delta-doped layer," Applied Surface Science **203-204**, 62–68 (2003).
24. A. Kalnitsky, S. P. Tay, J. P. Ellul, S. Chongsawangvirod, J. W. Andrews, and E. A. Irene, "Measurements and modeling of thin silicon dioxide films on silicon," J. Electrochem. Soc. **1**, 234–238 (1990).
25. Y. Wang and E. A. Irene, "Consistent refractive index parameters for ultrathin SiO_2 films," J. Vac. Sci. Technol. B **18**, 279–282 (2000).

1. Introduction

Although digital holographic microscopy (DHM) allows the measurement of the entire complex optical wavefront [1], up to now only the phase signal is really exploited for quantitative measurement. Indeed, for reflection configurations, the phase signal is converted into topography under homogeneous material and single reflection interface assumption [1, 2, 3]; and

#121163 - $15.00 USD Received 8 Dec 2009; revised 2 Feb 2010; accepted 3 Feb 2010; published 5 Feb 2010

into thickness and/or refractive index (RI) in transmission configurations [4, 5, 6, 7, 8, 9]. On contrary, in reflectance measurement systems, like time spectral interferometry, thin film thicknesses and RI are only measured from the reflected wavefront intensities [10, 11]. Recently, Debnath *et al.* used a spectrally-resolved phase-shifting interferometer to measure thicknesses of thin transparent layers [12] thicker than 100 nm [13]. In this paper, quantitative complex data measured by dual-wavelength DHM allows the measurement of thiner layers in addition to topography and/or RIs for non-homogeneous multiple layer samples. For this purpose, a theoretical complex function (amplitude and phase), describing the reflected wave propagation through multiple layers, is established. In addition to standard models, our function models the sources coherence lengths, usually chosen in the hundreds of micrometers range in order to reduce parasitic interferences contributions. Topography, thicknesses and RIs determination using this function is demonstrated on home-made SiO_2 test targets and different types of SIMS sputter craters on multiple layers.

2. DHM setup

Figure 1 presents the basic configuration of the dual-wavelength DHM used for the experimental validation and demonstration of the DHM reflectometry. This DHM (DHM R1100® from Lyncée Tec) has two different wavelength sources (682.5 nm and 660 nm, with respective coherence length (L_c) of 300 μm and 600 μm, that can be switched on and off alternately to provide two different 1024×1024 pixels holograms recorded on the CCD camera, resulting from the interference between the reference wave and the object wave reflected by the specimen. Usually, dual-wavelength DHM is used to increase the vertical measurement range by an extension of the phase ambiguity-free phase measurement range obtained on homogeneous material and single reflection samples [14]. This ambiguity can also appear for multiple reflections. Furthermore, a dual-wavelength DHM doubles the equation numbers for the fitting procedure explained further. A microscope objective (MO) is used to improve the lateral resolution (LR), that is diffraction limited and depends on the numerical aperture (NA) of MO (LR$= 0.61\lambda/$NA) as in classical microscopy [15]. All results in this paper are achieved with a 10× MO (NA$= 0.3$) that gives a lateral resolution about 1.4μm. The condenser lens (CL in Fig. 1) focalizes the wave near the back focal plane of the MO to deliver a collimated illuminating wave Ψ_{ill}. The optical path length (OPL) of the reference wave is adjusted by moving the optical path retarder (OPR). The maximal coherence plane, defined in Fig. 2, is placed on the sample surface at the position $x_0 = 0$ by calibrating the position of the OPR to have a maximal fringe contrast when the surface of a calibration mirror is focalized.

3. Complex wavefront measurement

For each wavelength λ_i, the hologram intensities are

$$I_{Hi} = |R_i|^2 + |O_i|^2 + R_i O_i^* + R_i^* O_i, \tag{1}$$

where R_i and O_i are respectively the reference and object waves for the wavelength λ_i. These digital holograms are filtered in the spatial frequency domain by using the technique explained in details in Ref. [16], to retain the real image term $R_i O_i^*$ (in reflection it corresponds to the topographic contrast, a hole giving a phase decrease).

Due to the finite coherence length of the source and due to non-perfecting homogeneous reference and object waves intensities on the CCD, the reconstructed amplitude is not homogeneous in the field of view when using a standard reconstruction. Therefore, a spatial amplitude normalization is performed using a reference hologram recorded on a flat reference surface (mirror) as specimen. This hologram is filtered to keep its $R_i O_{i,ref}^*$ term. The normalization of

#121163 - $15.00 USD Received 8 Dec 2009; revised 2 Feb 2010; accepted 3 Feb 2010; published 5 Feb 2010

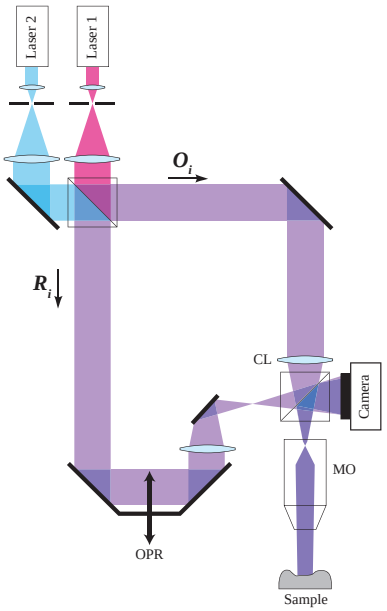

Fig. 1. DHM R1100® setup. Two lasers sources can be alternatively switched on. The object wave O_i passes through a condenser CL and a microscope objective MO to illuminate the sample with a collimated beam. The reflected wave interferes with the reference wave R_i, whose optical path length can be adjusted with the optical path retarder OPR.

the phase [17], but also of the amplitude [3], is performed using the normalization reference hologram

$$\Gamma_H = \frac{1}{\left|R_i O^*_{i,ref}\right|} \exp\left(-i\phi_{i,ref}\right), \tag{2}$$

that multiplies the filtered object hologram:

$$\Psi_{i,H} = \Gamma_H R_i O^*_{i,ref} = \frac{|O_i|}{|O_{i,ref}|} \exp[i(\phi_i - \phi_{i,ref})]. \tag{3}$$

$\Psi_{i,H}$ is then numerically propagated to the focus plane to obtain Ψ_i. The numerical propagation is computed in the convolution formalism, with the use of numerical lenses to compensate for possible aberrations, as described in details in Ref. [18]. The numerical reconstruction of the digital complex wavefront for 1024×1024 pixels hologram is done in less than 1/30 second.

One should note that Ψ_i can be different from the effective optical object wave. Indeed, for a single reflection on a sample surface, the amplitude of Ψ_i is clearly dependent on the position of the OPR due to the finite coherence length of the sources. In fact the recorded wave is different from the real wave and corresponds to

$$\Psi_{i,H} = g(\mathrm{OPL}, \mathrm{OPR}) R_i O^*_i, \tag{4}$$

where $g(\mathrm{OPL}, \mathrm{OPR})$ is the degree of coherence function that is defined by the Gaussian function:

$$g(\mathrm{OPL}, \mathrm{OPR}) = \exp\left[-\frac{(\mathrm{OPL} - \mathrm{OPR})^2}{2\sigma^2}\right], \tag{5}$$

#121163 - $15.00 USD Received 8 Dec 2009; revised 2 Feb 2010; accepted 3 Feb 2010; published 5 Feb 2010

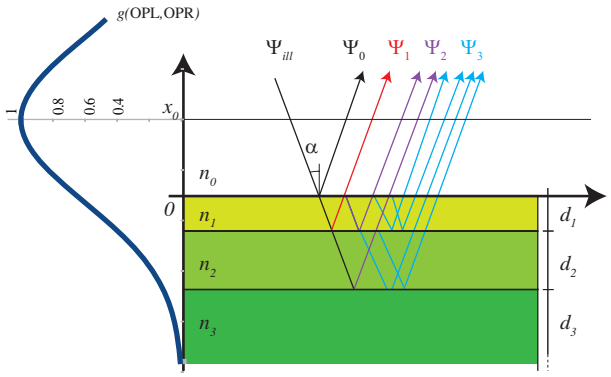

Fig. 2. Multilayer schematic. Ψ_{ill} is the illumination wave, (experimentally $\alpha = 0$), and Ψ_r (r=0,...) are the multiple reflections of order r. x_0 is the position that corresponds to the Gaussian center of the degree of coherence function $g(\mathrm{OPL},\mathrm{OPR})$.

with the coherence length L_c of the source defined as

$$L_c = 2\sigma(2\ln 2)^{1/2}. \tag{6}$$

Here with multiple layer samples, as the degree of coherence influences the summation of the multiple reflected wave, it has to be taken into account. It is not the case in usual reflection DHM where the topography is proportional to the phase.

4. General equation of reflected complex wave on a three interfaces sample

Two different equivalent methods are usually used to model reflected wave propagation through multiple layers: the infinite summation of Fresnel amplitudes and the transfer-matrix method. The reader can refer to Ref. [19] to have more details about the two techniques. In this paper, a modified version of the infinite summation is developed to take the influence of the coherence length into account.

Figure 2 presents the schematic principle. The illumination wave Ψ_{ill} has a normal incidence because a collimated illumination beam is used ($\alpha = 0$). Ψ_{ill} is depicted with an angle for didactic purpose to separate the different multiple reflections on the 3 layers with respective complex RI n_k and thickness d_k ($d_3 = \infty$). We deliberately choose to present only a 3 interfaces model to lighten the equations and because we will study sample with a maximum of 3 interfaces. The model can be generalized for more layers.

The reflection and transmission Fresnel coefficients on interface kl are, for $\alpha = 0$

$$r_{kl} = (n_k - n_l)/(n_k + n_l), \tag{7}$$
$$t_{kl} = 2n_k/(n_k + n_l). \tag{8}$$

The different contributions to the reflected wave are in $x = 0$

$$\begin{aligned}
\Psi_0 &= r_{01}g(0,\mathrm{OPR}),\\
\Psi_1 &= t_{01}r_{12}t_{10}\exp\left(i\frac{2\pi}{\lambda}2d_1n_1\right)g[\Re(2d_1n_1),\mathrm{OPR}]\\
&= Tg'(X),\\
\Psi_2 &= t_{01}r_{12}r_{10}r_{12}t_{10}\exp\left(i\frac{2\pi}{\lambda}4d_1n_1\right)g[\Re(4d_1n_1),\mathrm{OPR}]
\end{aligned}$$

#121163 - $15.00 USD Received 8 Dec 2009; revised 2 Feb 2010; accepted 3 Feb 2010; published 5 Feb 2010

$$
\begin{aligned}
&+ \quad t_{01}t_{12}r_{23}t_{21}t_{10}\exp\left[i\frac{2\pi}{\lambda}(2d_1n_1+2d_2n_2)\right]g[\Re(2d_1n_1+2d_2n_2),\mathrm{OPR}]\\
&= \quad ATg'(2X)+BTg'(X+Y),\\
\Psi_3 &= \quad t_{01}r_{12}r_{10}r_{12}r_{10}r_{12}t_{10}\exp\left(i\frac{2\pi}{\lambda}6d_1n_1\right)g[\Re(6d_1n_1),\mathrm{OPR}]\\
&+ \quad t_{01}r_{12}r_{10}t_{12}r_{23}t_{21}t_{10}\exp\left[i\frac{2\pi}{\lambda}(4d_1n_1+2d_2n_2)\right]g[\Re(4d_1n_1+2d_2n_2),\mathrm{OPR}]\\
&+ \quad t_{01}t_{12}r_{23}t_{21}r_{10}r_{12}t_{10}\exp\left[i\frac{2\pi}{\lambda}(4d_1n_1+2d_2n_2)\right]g[\Re(4d_1n_1+2d_2n_2),\mathrm{OPR}]\\
&+ \quad t_{01}t_{12}r_{23}r_{21}r_{23}t_{21}t_{10}\exp\left[i\frac{2\pi}{\lambda}(2d_1n_1+4d_2n_2)\right]g[\Re(2d_1n_1+4d_2n_2),\mathrm{OPR}]\\
&= \quad A^2Tg'(3X)+ABTg'(2X+Y)+BCTg'(2X+Y)+BDTg'(X+2Y), \qquad (9)
\end{aligned}
$$

where $\Re$ is the complex real part, $T = t_{01}r_{12}t_{10}$, $\mathrm{OPR} = 2x_0n_0$, $g'(x) = g[\Re(x),\mathrm{OPR}]\exp\left[i\frac{2\pi}{\lambda}(x)\right]$, $X = 2d_1n_1$, $Y = 2d_2n_2$, $A = r_{12}r_{10}$, $B = t_{12}r_{23}t_{21}/r_{12}$, $C = r_{10}r_{12}$ and $D = r_{21}r_{23}$. One can note that a simple rule allows deducing the component Ψ_{r+1} from Ψ_r:

$$
\begin{aligned}
\Psi_r &\rightarrow \Psi_{r+1}\\
\ldots ATg'(mX+nY) &\rightarrow \begin{cases} \ldots AATg'[(m+1)X+nY] \\ \ldots ABTg'[mX+(n+1)Y] \end{cases}\\
\ldots BTg'(mX+nY) &\rightarrow \begin{cases} \ldots BCTg'[(m+1)X+nY] \\ \ldots BDTg'[mX+(n+1)Y] \end{cases}\\
\ldots CTg'(mX+nY) &\rightarrow \begin{cases} \ldots CATg'[(m+1)X+nY] \\ \ldots CBTg'[mX+(n+1)Y] \end{cases}\\
\ldots DTg'(mX+nY) &\rightarrow \begin{cases} \ldots DCTg'[(m+1)X+nY] \\ \ldots DDTg'[mX+(n+1)Y] \end{cases} \qquad (10)
\end{aligned}
$$

The wavefront in $x = x_0$ is therefore:

$$
\Psi(\mathbf{d},\mathbf{n},x_0) = \left[\sum_{r=0}^{N}\Psi_r\exp\left(i\frac{2\pi}{\lambda}2x_0n_0\right)\right]^* = \sum_{r=0}^{N}\Psi_r^*\exp\left(-i\frac{2\pi}{\lambda}2x_0n_0\right) \qquad (11)
$$

where $\mathbf{d} = [d_1, d_2]$ and $\mathbf{n} = [n_0, n_1, n_2, n_3]$. One can note the complex conjugate operator in the summation, in order to stay consistent with the real image term reconstruction.

5. Models and fitting procedure

The previous section presents the general function of the wave reflected on a three interfaces sample. But for each point of a micro-structure, the parameters of this function could be different, and a model of the micro-structure has to be defined. In the next sections, we present two different example of micro-structures model: steps deposition on a single layer wafer, and etching on 3 interfaces samples. These models, combined with fitting procedure, allow the measurement of topographic image of two home-made SiO_2 /Si test targets and SIMS sputter craters in multiple interface sample.

5.1. Structured deposition on a single layer

Figure 3 presents the model for a micro-structure of height $h(x,y)$ and RI n_d deposited on a wafer composed of a semi-infinite layer ($d_2 = \infty$) and RI n_w. The theoretical function (Eq. 11)

#121163 - $15.00 USD Received 8 Dec 2009; revised 2 Feb 2010; accepted 3 Feb 2010; published 5 Feb 2010

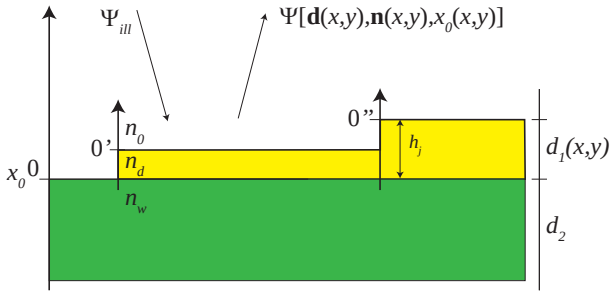

Fig. 3. Model for structures of height $h(x,y)$ and RI n_d deposited on a semi-infinite wafer ($d_2 = \infty$) with RI n_w. The multiple layers function (Eq. 11) is defined from the respective origin 0, 0' and so on, for each step.

is now adapted to this model. For each position (x,y) of the sample, the reflected wavefront is

$$\Psi(x,y) = \Psi[\mathbf{d}(x,y),\mathbf{n}(x,y),x_0(x,y)] \tag{12}$$

where the different parameters depend on the deposit thickness $h(x,y)$:

$$\mathbf{d}(x,y) = [h(x,y),\infty] \tag{13}$$

$$\mathbf{n}(x,y) = \begin{cases} [n_0,n_w,0,0] \text{ if } h(x,y)=0 \\ [n_0,n_d,n_w,0] \text{ if } h(x,y)>0 \end{cases} \tag{14}$$

$$x_0(x,y) = -h(x,y). \tag{15}$$

5.2. *Etching in multiple layers*

Figure 4 presents the model for an etching dug in a 3-layers wafer of respective RI and thickness (n_k, d_k, $k = 1$ to 3, $d_3 = \infty$). For each position (x,y) of the sample, the reflected wavefront $\Psi(x,y)$ (Eq. 12) is this time defined by the parameters:

$$\mathbf{d}(x,y) = \begin{cases} [d_1+h(x,y),d_2] \text{ if } -h(x,y) < d_1 \\ [d1+d_2+h(x,y),\infty] \text{ if } d_1 < -h(x,y) < d_1+d_2 \\ [\infty,\infty] \text{ if } d_1+d_2 < -h(x,y) \end{cases} \tag{16}$$

$$\mathbf{n}(x,y) = \begin{cases} [n_0,n_1,n_2,n_3] \text{ if } -h(x,y) < d_1 \\ [n_0,n_2,n_3,n_3] \text{ if } d_1 < -h(x,y) < d_1+d_2 \\ [n_0,n_3,n_3,n_3] \text{ if } d_1+d_2 < -h(x,y) \end{cases} \tag{17}$$

$$x_0(x,y) = -h(x,y). \tag{18}$$

where $h(x,y) < 0$ is the crater depth.

5.3. *Fitting procedure*

5.3.1. Normalization

A first normalization to compensate for aberrations and for non-homogeneity of wavefronts intensities, is achieved by the use of a reference hologram recorded in an assumed flat area of the investigated sample, by using the procedure explained in Section 3. But, it is still necessary to compensate for phase offset variations due to external vibrations. This task is achieved by computing the mean phase value $\phi_{exp}(h=0)$ in an assumed homogeneous Region of Interest (ROI) corresponding to $h = 0$ (for example dashed rectangle in Fig. 5(b); and to suppress it to the experimental wavefront Ψ_{exp}. The theoretical model function $\Psi(x,y)$ is also normalized with

#121163 - $15.00 USD Received 8 Dec 2009; revised 2 Feb 2010; accepted 3 Feb 2010; published 5 Feb 2010

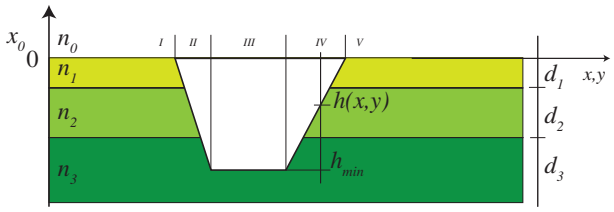

Fig. 4. Etching dug in 3-layers wafer model. The maximum coherence position is $x_0 = 0$. The etching is delimited by 5 different areas (I,V: outside crater; II and IV crater edges; and III maximum depth). The layers are defined by the RIs n_k and thicknesses d_k.

the complex value computed for $h = 0$. The normalized experimental and theoretical functions are:

$$\bar{\Psi}_{exp}(x,y) = \Psi_{exp}(x,y)\exp[-i\phi_{exp}(h=0)], \tag{19}$$

$$\bar{\Psi}(x,y) = \frac{\Psi(x,y)}{\Psi(h=0)}. \tag{20}$$

5.3.2. Mean square fitting

For a given type of sample, the normalized theoretical functions $\bar{\Psi}_i$ (i=1,2 for respectively λ_1 and λ_2) are defined by the thicknesses and RIs. These parameters can be either a priori known constants or the results of a previous fitting procedure. Furthermore, some parameters are assumed to be identical in the entire field of view (for example thickness and RIs), on contrary to the topography (deposit structure height, etching depth) that depends on the position (x,y). Therefore, to determine the unknown parameters, $2S$ experimental data points ($\bar{\Psi}_{i,exp}$) (S for each wavelength) are fitted by minimizing the sum of errors between theoretical and experimental complex data (errors corresponds to the distances between the complex vectors in the complex plane):

$$\mathrm{MSE} = \sum_{i=1}^{2}\sum_{j=1}^{S}\left|\bar{\Psi}_{ij} - \bar{\Psi}_{ij,exp}(\mathbf{d},\mathbf{n})\right|, \tag{21}$$

where the subscript ij correspond to the wavelength λ_i and the step j. MSE is therefore the mean square error of the fit. It implies that the system has to be determined or overdetermined to find a solution. Therefore, it is not possible, in the most general cases, to compute all the parameters. But in most of the cases, several parameters can be computed as it will be demonstrated in the next sections.

As fitting procedures are time consuming tasks and as RIs and thickness layers can be considered most of the time as constant, the mean square fitting is achieved by only taking into account complex data averaged over selected ROIs. These constants then allow computing the topography for each image pixel by using the next procedure. One has to note that, constant

5.3.3. Topographic image

When RIs and layer thicknesses are assumed to be known constants on the entire field of view (known sample characteristics or fitting results), the theoretical complex functions $\bar{\Psi}_i(h)$ are computed with $h = h_{min} + p\Delta h$, $p = 0,N$ (Δh defines the precision, h_{min} the minimal height, N the number of points). Then for each reconstructed pixel (x,y), the height $h(x,n)$ is defined as the abscissa that corresponds to the minimum of the function $\sum_{i=1}^{2}\left|\bar{\Psi}_i(h) - \bar{\Psi}_{i,exp}(x,y)\right|$.

#121163 - $15.00 USD Received 8 Dec 2009; revised 2 Feb 2010; accepted 3 Feb 2010; published 5 Feb 2010

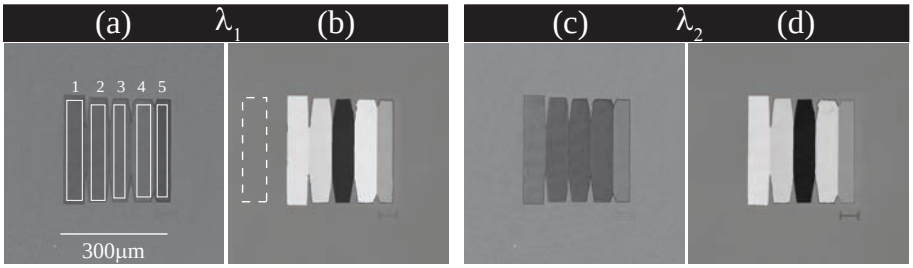

Fig. 5. Test target reconstructed wavefronts (a,c) amplitude and (b,d) phase images for λ_1 (a,b) and λ_2 (c,d). Steps are manufactured to be nominally 375, 525, 975, 1200 and 1275 nm high. The rectangles in (a) correspond to the ROIs used for the spatial averaging of complex data for RIs determination, the dashed rectangle in (b) defines the ROI used for the phase normalization.

6. Results

6.1. *Structured deposition on single layer*

Two home-made test targets, composed of different thickness steps of SiO_2 deposited on a Si wafer, are measured by DHM reflectometry. The first target is composed of low resolution (LR) steps of 375, 525, 975, 1200 and 1275 nm in thickness and the second one is composed of high resolution (HR) steps of 25, 35, 65, 80 and 85 nm in thickness (fabrication precision is about $\pm$3%).

Figure 5 presents the reconstructed complex data achieved with the two wavelengths. One can note that the normalization described in Eq. 19 is achieved by computing $\exp[-i\phi_{exp}(h = 0)]$ as the averaging phase value acquired in the dashed rectangle area defined in Fig. 5(b).

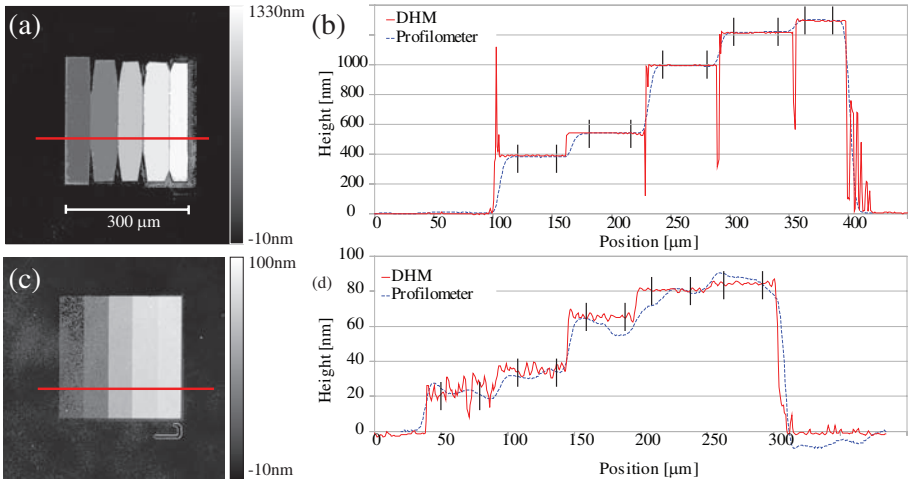

Fig. 6. Topography of (a) low, and (c) high resolution test targets; (b, d) respective profiles comparison between DHM [8 pixels average profile along red line in (a,c)] and Tencor Alphastep 200 profilometer. The standard deviations between the vertical lines are used to define the uncertainty in Table 1.

#121163 - $15.00 USD Received 8 Dec 2009; revised 2 Feb 2010; accepted 3 Feb 2010; published 5 Feb 2010

6.1.1. Refractive index determination

For these samples, the model defined in Fig. 3 is used with $n_0 = n_{air} = 1$, $n_d = n_{SiO_2}$. As the deposition parameters (temperature, pressure, deposition rate, and so on) influence the RI of wafer and deposit [20], we will use the first target with the larger height differences to determine the RIs, enabling then the measurement of the step heights for the two targets (the second target was manufactured with same deposition parameters). As the RIs are assumed homogeneous and to reduce the computation time, the least square fitting for the real RI determination (the imaginary RI is neglected) is carried with the average complex data contained in ROIs [white rectangles on Fig. 5(a)] and gives $n_{Si0_2} = 1.4706$ and $n_{Si} = 3.8051$.

6.1.2. Step heights determination

In order to validate the step height measurements, profiles measured with a Tencor Alphastep 200 stylus profilometer are compared to DHM reflectometry measurements. They are two different ways to measure the step heights: either the mean ROI values are considered (column DHM ROI in Table 1), or the topographic images [Fig. 6(a,c)] are computed as explained in Section 5.3.3. The extracted profiles are compared with profilometer results [Fig. 6(b,d)]. For DHM ROI, no uncertainty is defined as the fit is obtained on the average complex value on the entire step. On contrary, with the profiles extraction, the uncertainty for the profilometer and for DHM is defined similarly by the addition of the standard deviation of the measurement along a profile taken in assumed flat area, and the standard deviation of the profile values between the vertical lines for each step in Fig. 6(b) in an assumed flat area.

Table 1. Comparison between theoretical step height and their measurement with DHM reflectometry and stylus profilometer

Target	Parameters		Theory	DHM ROI	DHM Profile	Profilometer
	n_{Si0_2}	[-]	1.4556*	1.4706	-	-
	n_{Si}	[-]	3.8054**	3.8051	-	-
	h_1	[nm]	375 ± 11.3	388.8	389.9 ± 2.8	379.7 ± 3.9
LR	h_2	[nm]	525 ± 15.8	539.4	541.0 ± 2.3	542.3 ± 4.1
	h_3	[nm]	975 ± 29.3	995.8	997.3 ± 2.9	994.6 ± 5.1
	h_4	[nm]	1200 ± 36.0	1216.7	1216.8 ± 2.8	1220.2 ± 5.8
	h_5	[nm]	1275 ± 38.3	1293.8	1296.1 ± 3.0	1300.7 ± 4.9
	h_1	[nm]	25 ± 0.8	23.1	22.6 ± 5.7	22.5 ± 3.9
	h_2	[nm]	35 ± 1.1	35.5	35.0 ± 2.1	32.2 ± 4.7
HR	h_3	[nm]	65 ± 2.0	65.0	65.5 ± 1.1	59.5 ± 6.7
	h_4	[nm]	80 ± 2.4	80.3	80.7 ± 0.6	78.8 ± 5.7
	h_5	[nm]	85 ± 2.6	83.8	84.5 ± 0.7	87.8 ± 4.3

LR, low resolution; HR, high resolution target; Theory, theoretical refractive indices and step heights; DHM ROI, fit of the RIs n_{Si0_2} and n_{Si} and heights from complex values averaged over ROIs; DHM Profile, step height measured from the profile defined in Fig. 6. Theoretical RIs are defined from Ref. [21] and for * 688.8nm and **681.2nm.

6.2. SIMS sputter crater

Secondary Ion Mass Spectrometry (SIMS) is an outstanding analytical technique for surface characterization and in-depth information with applications in a broad range of scientific and industrial fields [22]. In this work we used a TOF.SIMS^5 instrument (IONTOF, Germany), in order to prepare craters of different depths via sputtering with O_2^+ (Energy: 1 keV, sputter current: 254 nA). For SIMS data treatment, it is of major importance to obtain the accurate

#121163 - $15.00 USD Received 8 Dec 2009; revised 2 Feb 2010; accepted 3 Feb 2010; published 5 Feb 2010

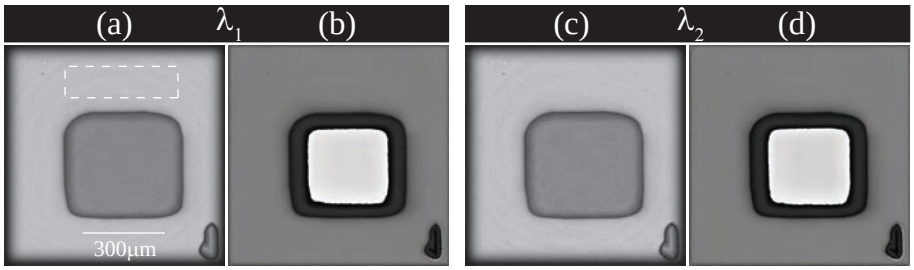

Fig. 7. 3-layers (Au/SiO_2/Si) SIMS sample reconstructed wavefronts (a,c) amplitude and (b,d) phase images for λ_1 (a,b) and λ_2 (c,d). The dashed rectangle in (a) delineates the ROI used for phase normalization.

depth of sputter craters [23]. Here we demonstrate the capability of DHM reflectometry in order to provide this information even for samples which include thin transparent layers.

The first analyzed crater is sputtered in a 3 interfaces wafer composed of gold ($n_1 = 0.161 + 3.445812i$ @670.2 nm, $d_1 = 40$ nm), SiO_2 ($n_2 = 1.4560$ @670 nm, $d_2 = 100$ nm) and finally a Si substrate ($n3 = 3.815103 + 0.014041i$ @673.8 nm). The RIs around 670nm is used as the average RIs for 660nm and 680nm. From Ref. [21], the theoretical RI differences between the source wavelengths and the used RI at about 670nm are below 0.001 for SiO_2, 0.02 for Si and 0.004 for Au. As the deposit process can shift the RI with higher magnitude [20], this difference is negligible for topographic determination.

From the measured complex data presented in Fig. 7, the topographic image [Fig. 8(a)] enables to compare the depths obtained with DHM (-252.8 ± 1.9 nm) and the profilometer (-249.3 ± 5.4 nm).

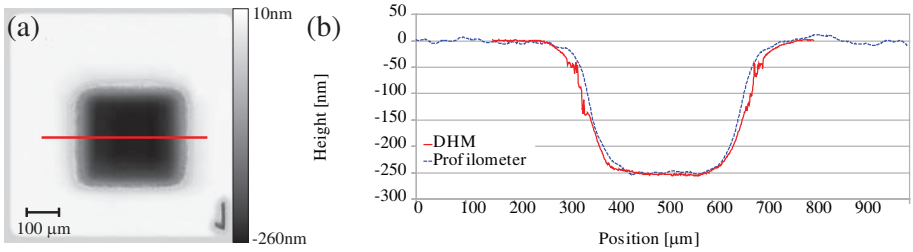

Fig. 8. (a) Topographic image of SIMS crater sputtered in three layers of 40 nm Au, 100 nm SiO_2 and Si; (b) profile comparison between DHM [8 pixels average profile along red line] and Tencor Alphastep 200 profilometer.

Now, two different SiO_2 layer thicknesses wafer (certified 35 and 100 nm) with sputtered craters are investigated. The reconstructed amplitude and phase images for λ_1 are presented in Fig. 9.

As for RIs determination, the layer thicknesses are computed by the mean square fitting of average values in ROIs (white rectangles in Fig. 9), with layer thickness and depth as parameters. The fit gives respectively $d_1 = 103$ nm, $h_{min} = -226.7$ nm and $d_1 = 33.7$ nm, $h_{min} = -148.8$ nm. From the computed thicknesses and theoretical RIs, the topographic images [Figs. 10(a,c)], and the respective profiles are computed and compared to profilometer [Fig. 10(b,d)].

#121163 - $15.00 USD Received 8 Dec 2009; revised 2 Feb 2010; accepted 3 Feb 2010; published 5 Feb 2010

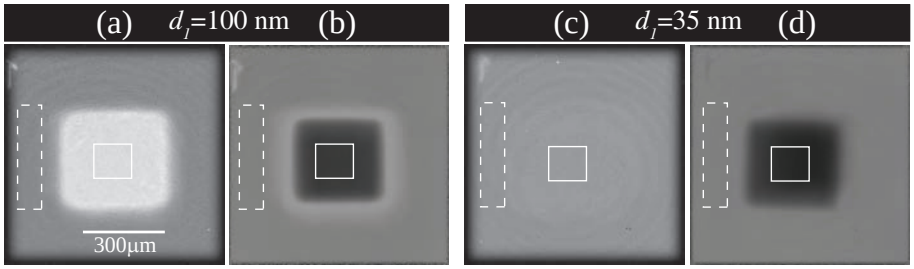

Fig. 9. SIMS sample reconstructed wavefronts (a,c) amplitude and (b,d) phase images for λ_1. The SiO_2 layer thicknesses are assumed to be respectively (a,b) 100 nm and (c,d) 35 nm. The dashed rectangles delineate the ROI used for the spatial averaging for the phase normalization and the plain line rectangles define the ROI for bottom crater average values.

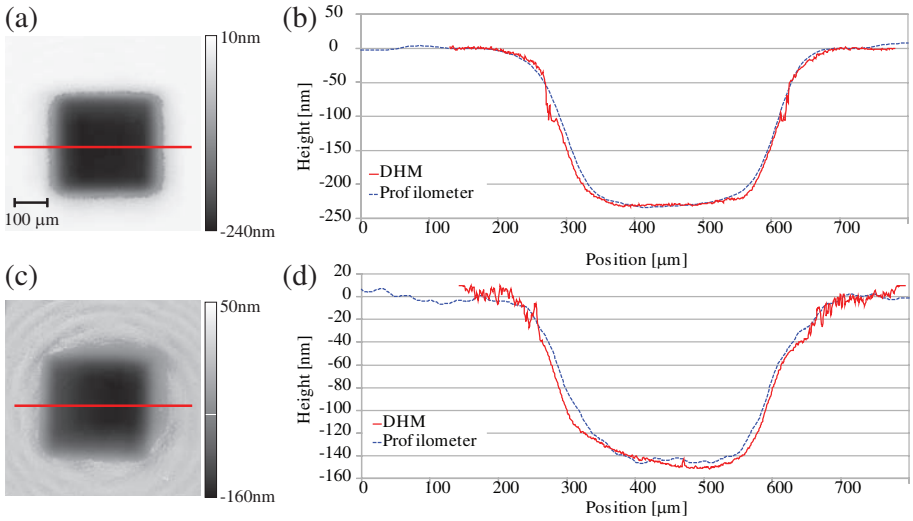

Fig. 10. (a,c) Topographic images of SIMS crater sputtered in two layers of (a) 100 nnm and (c) 35 nm SiO_2 and Si; (b,d) profiles comparison between DHM [8 pixels average profile along red line] and Tencor Alphastep 200 profilometer.

7. Results discussion

Measured and theoretical RIs (Table 1) are in very good agreement. The error on Si RI is smaller than 10^{-3} and for the deposit SiO_2 smaller than 2×10^{-2}. The larger difference for SiO_2 RI can be explained by two reasons. The SiO_2 RI depends on the deposition procedure [20] and on thickness for thin layer (0-10 nm) [24, 25].

The stylus profilometer and DHM reflectometry measurements are also in very good agreement as shown in Figs. 6, 8 and 10. In Table 1, only the first LR step height uncertainties do not overlap for 3.5 nm. That can be explained if profiles are not taken exactly in the same position, in addition with some other error sources. First, the noise on the complex wavefront measurement (residual parasitic interferences, shot noise, and so on) has influence on height measurement, and especially on thiner layer as shown in the HR target of Table 1, where the incertitude for the smallest step is about 2.5 times larger than the higher ones of HR target. One can also note the same behavior in Figs. 10(c,d), where small depths that correspond to thin SiO_2 layer are noisier; especially the concentric pattern on reconstructed amplitude [Fig. 9(c)],

#121163 - $15.00 USD Received 8 Dec 2009; revised 2 Feb 2010; accepted 3 Feb 2010; published 5 Feb 2010

coming from a parasitic interference, gives an important contribution in the reconstructed depth field [Fig. 10(c)]. This problem is inherent to the DHM setup configuration. Reduced coherence length, small misalignment of optics or numerical spatial filtering could permit to avoid most of these parasitic interferences. Nevertheless, it is very difficult to avoid all of them, especially for a DHM microscope configured with a turret of several magnification MO.

Secondly, an error on the RI determination for the reasons previously given, contributes also to a mismatch between real and measured heights. This effect could also explain the abrupt and noisier transition near layer interfaces in graphs (c,d) of Figs. 8 and 10. Finally, the non dispersion assumption and normal incident wave contributes to increase the uncertainty. An advantage of DHM can be seen in Fig. 6(d), where step edges are sharper for DHM reflectometry than for profilometer. Indeed the stylus tip size induces rounded edges transition. Furthermore, DHM has the advantage to avoid mechanical calibration to convert detected signal in height, on contrary of profilometer or AFM instruments; DHM calibration depends only on the wavelength sources.

Finally, the measured layer thicknesses of SiO_2 from the SIMS sample (Fig. 10) coincide very well with the certified values (33.7 nm and 103 nm for 35 nm and 100 nm certification). The difference can be explained by the same arguments as before: complex data noise, mismatch between real and used RI.

One notes that the DHM reflectometry principle is demonstrated for a small magnification MO ($10\times$). For higher magnification, the basic principle is still valid if the illumination wave could still be assumed collinear. If this assumption could not be satisfied, the incident angles should be in the theoretical equation. Furthermore, for high NA, the depth-of-focus (DOF) limits the precision for layer thickness larger or near the DOF. Indeed, the waves reflected from interfaces out of DEF gives an out-of-focus contribution that can be eventually shifted compared to the first interface if the sample is not perpendicular to the optical axis.

Next improvements for DHM reflectometry will be to introduce dispersion and incident angles in the theoretical equation, in particular for high magnification application. Furthermore, simultaneous dual-wavelength DHM will allow to obtained real-time measurements. Three or more wavelengths will also permit to increase the number of equations and therefore the numbers of unknown parameters to fit simultaneously, in particular the thickness for all layers. Obviously, the increase of unknown parameters, for a given number of equations, increases the fitting time consuming exponentially and decreases the precision on the fitting parameters.

8. Conclusion

These results show that DHM reflectometry allows full field topographic thickness of semi-transparent layers micro-structures, with a resolution better than 2 nm for layer larger than 20-30 nm. Furthermore, we demonstrate that DHM reflectometry allows RIs determination with a precision better than 2×10^{-2} for the deposited material RI and 1×10^{-3} for the wafer RI. With this new DHM measurement modality, surface topography of both homogeneous and non-homogeneous material samples are measured precisely. This opens new application fields for DHM, like thin films and multiple material specimen investigation.

Acknowledgments

The research leading to these results has received funding from the European Community's Seventh Framework Programme FP7/2007-2013 under grant agreement n^o 216105. The authors thank Bamdad Afra from the Advanced Photonics Laboratory in EPFL (Ecole Polytechnique Fédérale de Lausanne) for the delivery of the stylus profilometer measurements. Ahmet Ata Akatay is supported by the CCMX NMMC grant: "Study of complex interfacial properties with nanoscale resolution optical microscopy".

#121163 - $15.00 USD Received 8 Dec 2009; revised 2 Feb 2010; accepted 3 Feb 2010; published 5 Feb 2010